The Astrophysical Journal, 974:232 (9pp), 2024 October 20 https://doi.org/10.3847/1538-4357/ad6f9b

The Rise of the *r*-process in the Gaia-Sausage/Enceladus Dwarf Galaxy*

Xiaowei Ou (欧筱葳)[1], Alexander P. Ji[2,3], Anna Frebel[1], Rohan P. Naidu[1,5], and Guilherme Limberg[4]
[1] Department of Physics and Kavli Institute for Astrophysics and Space Research, Massachusetts Institute of Technology, 77 Massachusetts Avenue, Cambridge, MA 02139, USA; xwou@mit.edu
[2] Department of Astronomy & Astrophysics, University of Chicago, 5640 S. Ellis Avenue, Chicago, IL 60637, USA
[3] Kavli Institute for Cosmological Physics, University of Chicago, Chicago, IL 60637, USA
[4] Universidade de São Paulo, Instituto de Astronomia, Geofísica e Ciências Atmosféricas, Departamento de Astronomia, SP 05508-090, São Paulo, Brazil
Received 2024 April 12; revised 2024 August 12; accepted 2024 August 13; published 2024 October 15

Abstract

Neutron star mergers (NSMs) produce *r*-process elements after a time-delayed inspiral process. Once a significant number of NSMs are present in a galaxy, *r*-process elements, such as Eu, are expected to significantly increase with time. Yet, there have been limited observational data in support of Eu increasing within Local Group galaxies. We have obtained high-resolution Magellan/MIKE observations of 43 metal-poor stars in the Gaia-Sausage/Enceladus (GSE) tidally disrupted galaxy with $-2.5 < [Fe/H] < -1$. For the first time, we find a clear rise in [Eu/Mg] with increasing [Mg/H] within one galaxy. We use a simple chemical evolution model to study how such a rise can result from the interplay of prompt and delayed *r*-process enrichment events. Delayed *r*-process sources are required to explain the rise and subsequent leveling off of [Eu/Mg] in this disrupted galaxy. However, the rise may be explained by delayed *r*-process sources with either short (∼10 Myr) or long (∼500 Myr) minimum delay times. Future studies on the nature of *r*-process sources and their enrichment processes in the GSE will require additional stars in the GSE at even lower metallicities than the present study.

Unified Astronomy Thesaurus concepts: R-process (1324); Galactic archaeology (2178); Chemical enrichment (225)

Materials only available in the online version of record: machine-readable table

1. Introduction

The origin of rapid neutron-capture process (*r*-process) elements in the universe remains one of the most complex challenges in understanding the nucleosynthesis of all the elements across the periodic table (see, e.g., A. Frebel 2018; J. J. Cowan et al. 2021). The theoretical foundations of *r*-process nucleosynthesis have been known for several decades (E. M. Burbidge et al. 1957), but the details are still not all fully understood. The binary neutron star merger (NSM) event GW170817 provided the first direct evidence for NSMs as an astrophysical site for the operation of the *r*-process (e.g., D. Kasen et al. 2017; M. M. Kasliwal et al. 2017; M. R. Drout et al. 2017). Yet, it has been pointed out that NSMs may only be important at late(r) times due to delays induced by their binary evolution (e.g., A. Vigna-Gómez et al. 2018; B. Côté et al. 2018; P. Simonetti et al. 2019; P. Beniamini & T. Piran 2019; J. Lian et al. 2023). Rare types of core-collapse supernovae (rCCSNe) have been proposed as prompt *r*-process sources to account for early *r*-process production (e.g., C. Winteler et al. 2012; N. Nishimura et al. 2015; A. Frebel 2018; P. Mösta et al. 2018; D. M. Siegel et al. 2019; C. Kobayashi et al. 2020, 2023; J. J. Cowan et al. 2021; D. Yong et al. 2021) that appears to be required by observations of the many ancient metal-poor *r*-process-enhanced stars (E. M. Holmbeck et al. 2020; R. Ezzeddine et al. 2020; S. P. Shah et al. 2024).

Considering the chemical evolution of *r*-process elements within a galaxy, the differences in delay time distribution between prompt and delayed sources predict a potentially observable increase in *r*-process enhancement level as a function of time (F. Matteucci et al. 2014; G. Cescutti et al. 2015; G. E. Duggan et al. 2018; Á. Skúladóttir et al. 2019). If all *r*-process sources were prompt, the *r*-process element abundances, such as Eu, are expected to be constant relative to the α-element abundances, e.g., Mg, that are produced by prompt core-collapse supernovae (CCSNe). Delayed *r*-process sources, however, would cause the ratio of Eu to Mg abundances to increase as time passes/star formation progresses. While a comparison of [Eu/Mg] ratios in different galaxies suggested that the delayed *r*-process plays an important role (Á. Skúladóttir & S. Salvadori 2020; T. Matsuno et al. 2021; H. Reggiani et al. 2021; R. P. Naidu et al. 2022), clear evidence of a rise in [Eu/Mg] as a function of the metallicity within a single galaxy has been lacking. Instead, constant [Eu/Mg] ratios are observed in most Local Group galaxies, hinting that prompt sources could account for all *r*-process production (e.g., Á. Skúladóttir et al. 2019; M. Reichert et al. 2020), with the recent exception of Wukong (G. Limberg et al. 2024) and possibly also Ursa Minor (G. E. Duggan et al. 2018).

Gaining a better understanding of *r*-process sources and enrichment processes becomes possible with measurements of *r*-process abundances in stars that (1) span a significant range of metallicities, and (2) are associated with a common birth environment that we can clearly identify and characterize. These two conditions are both essential for establishing evidence of delayed sources but are challenging to achieve.

[5] NASA Hubble Fellow.
* This paper includes data gathered with the 6.5 meter Magellan Telescope located at Las Campanas Observatory, Chile.

For example, in the Milky Way, it is difficult to properly trace the galactic *r*-process content back to its sources because of its complex merger history (e.g., T. Tsujimoto & T. Shigeyama 2014; Y. Ishimaru et al. 2015; A. P. Ji et al. 2016), but stars at nearly all metallicities are accessible. However, efforts are underway from spectroscopic surveys such as the H3 survey (C. Conroy et al. 2019) to map out the merger history and trace the galactic *r*-process sources. On the other hand, for any intact dwarf galaxies, measurements of *r*-process abundances spanning a significant range in metallicities have proven challenging to obtain due to their distances ($\gtrsim$100 kpc) and corresponding faintness, and general low stellar masses ($\lesssim 10^6\,M_\odot$; A. Frebel & A. P. Ji 2023), although recent progress has been made with the Magellanic clouds at ∼50 kpc (H. Reggiani et al. 2021; A. Chiti et al. 2024; W. S. Oh et al. 2024).

To circumvent these challenges, recent studies have focused on numerous stars from merger debris of disrupted dwarfs ($\gtrsim 10^7\,M_\odot$) now found across the local halo of the Milky Way. In particular, the Gaia-Sausage/Enceladus (GSE, $M_\star \sim 10^{8.5}$–$10^{9.5}\,M_\odot$; A. Helmi et al. 2018; M. Haywood et al. 2018; V. Belokurov et al. 2018; J. M. D. Kruijssen et al. 2020; R. P. Naidu et al. 2020; G. Limberg et al. 2022) is one such system that is expected to have had a less complex merger history prior to merging with the Milky Way. The distinct, highly radial kinematics (orbital eccentricity $e \gtrsim 0.7$) and relatively close distances of the GSE stars allow their efficient identification for obtaining high-resolution spectroscopy. In addition, it is the Milky Way's most massive accretion event, with star formation lasting long enough (∼3.6 Gyr; A. Bonaca et al. 2020) to have likely experienced *r*-process enrichment from delayed sources.

Accordingly, a number of studies based on low- and high-resolution spectra of GSE stars have started to map out the chemical evolution of the GSE progenitor. Recent studies have focused on *r*-process elements, finding that GSE stars exhibit an overall enhancement in Eu abundances (D. S. Aguado et al. 2021; T. Matsuno et al. 2021; A. R. da Silva & R. Smiljanic 2023). R. P. Naidu et al. (2022) compared [Eu/Mg] ratios in both the GSE and Kraken stars (J. M. D. Kruijssen et al. 2020), two systems with similar stellar mass but different star formation duration. They argued that both rCCSNe and NSMs[6] are needed to explain the [Eu/Mg] abundances observed in the GSE population.

Previous studies, however, have failed to probe the early *r*-process enrichment process in the GSE, as samples had been restricted to [Fe/H] $\gtrsim -2.0$. As pointed out by R. P. Naidu et al. (2022), only stars with lower metallicity ([Fe/H] < -2) would have formed from gas dominantly enriched by prompt sources, such as rCCSNe.

In this study, we combine a new sample of metal-poor GSE stars with the existing GSE sample studied in R. P. Naidu et al. (2022) to extend the metallicity coverage to $-2.5 <$ [Fe/H] < -1.0. With 43 GSE stars in total, we consistently re-derive stellar parameters and chemical abundances with a particular focus on Eu and Mg, using Eu as a proxy for *r*-process enrichment and Mg as a proxy for the occurrence rate of CCSNe (Section 2). A clear rising trend in [Eu/Mg] abundances with metallicity is observed for the first time in the GSE (Section 3), confirming the existence of delayed *r*-process sources. We qualitatively explore the rate at which Eu is produced with a simple chemical evolution model invoking prompt and delayed sources and their different timescales (Section 4) based on the observed abundance trends. Such a rise is not observed in most other dwarfs (Section 5). Our results thus show that NSMs must have been present as a dominant site of *r*-process production in the GSE (Section 6).

[6] Following R. P. Naidu et al. (2022), we will refer to prompt (delayed) sources and rCCSNe (NSMs) interchangeably hereafter.

2. Observations and Analysis

The metal-poor GSE stars are selected following the same procedure described in R. P. Naidu et al. (2022). Briefly, stars are selected from APOGEE DR16 (H. Jönsson et al. 2020), the H3 survey (C. Conroy et al. 2019), and the Best & Brightest selection (K. C. Schlaufman & A. R. Casey 2014; V. M. Placco et al. 2019; G. Limberg et al. 2021) crossmatched with Gaia DR3 (Gaia Collaboration et al. 2021). Spectroscopic surveys provide line-of-sight velocities, while Gaia provides the coordinates, parallaxes, and proper motions. Dynamical quantities are then computed according to R. P. Naidu et al. (2020) using the default `MilkyWayPotential` from the GALA Python package (A. Price-Whelan et al. 2022).

We select GSE stars from APOGEE DR16 in the chemodynamical space using the following criteria:

$$\begin{aligned}(r_{\rm gal}/[{\rm kpc}] > 5) \wedge (e > 0.7)\\ \wedge [{\rm Mg/Mn}] > 0.25\\ \wedge [{\rm Mg/Mn}] - 4.25[{\rm Al/Fe}] > 0.55\\ \wedge E_{\rm tot}/[10^5\ {\rm km^2\ s^{-2}}] > -1.50.\end{aligned} \quad (1)$$

The [Mg/Mn] and [Al/Fe] space isolates the GSE accreted stars from the in situ Milky Way stars (K. Hawkins et al. 2015). The dynamical space selections are similar to those in the literature (e.g., G. Limberg et al. 2022; S. Buder et al. 2022).

For stars from the H3 survey, we select GSE stars as described in R. P. Naidu et al. (2020). For the Best & Brightest sample, we select GSE stars following the high-purity kinematics selection from D. K. Feuillet et al. (2020)

$$\begin{aligned}|J_\phi|/[{\rm kpc\ km\ s^{-1}}] < 500\\ \wedge J_r/[{\rm kpc\ km\ s^{-1}}] > 900\\ \wedge J_r/[{\rm kpc\ km\ s^{-1}}] < 2500.\end{aligned} \quad (2)$$

This more restrictive kinematics selection is adopted for the Best & Brightest sample because of a lack of independent elemental abundance information to remove in situ contaminants. In contrast, for the H3 and APOGEE samples, high-galactic-latitude survey selection and elemental abundances are available for in situ contaminants removal, allowing us to loosen the D. K. Feuillet et al. (2020) criterion.

Most importantly, we select stars with $T_{\rm eff} < 5000$ K. Targeted searches for metal-poor *r*-process-enhanced stars (e.g., E. M. Holmbeck et al. 2020; R. Ezzeddine et al. 2020) have shown that in metal-poor stars, Eu can only be measured in cool stars. A random selection of GSE members results both in primarily high-metallicity stars, as well as mostly warmer stars where Eu cannot be measured. Thus, it is crucial that we combine the GSE kinematics, low metallicity, and low $T_{\rm eff}$ criteria to select a sample suitable for studying *r*-process elements in the GSE.

To maximize the number of low-metallicity and cool GSE members, we search for GSE members with multiple different selection criteria from three different papers. Figure 1 shows

Table 1
Stellar Parameters, Final Derived Chemical Abundances, and Observing Information for 43 Stars Considered in This Study

Gaia DR3 Source ID	$T_{\rm eff}$	log g	[Fe/H]	$\sigma_{\rm [Fe/H]}$	[Mg I/H]	$\sigma_{\rm [Mg\ I/H]}$	[Eu II/H]	$\sigma_{\rm [Eu\ II/H]}$	[Eu II/Mg I]
31707926776039680	4896	1.89	−1.96	0.18	−1.63	0.12	−1.57	0.09	0.06
1187898485610541696	4451	1.53	−1.19	0.18	−0.95	0.14	−0.42	0.12	0.52
2472646349146818816	4593	1.51	−1.55	0.21	−1.21	0.12	−0.83	0.11	0.38
2504634406573540608	4814	2.15	−1.24	0.21	−1.00	0.14	−0.72	0.12	0.27
2505065101598396416	4488	1.49	−1.32	0.19	−1.03	0.14	−0.74	0.10	0.29

Note. The uncertainties listed include statistical and systematic uncertainties.
The complete version of Table 1 is available in the online edition of the journal. A short version with a subset of the columns is included here to demonstrate its form and content. The full table contains the following columns: Gaia DR3 Source ID, coordinates, observing details (date, binning, exposure time, and slit size), $T_{\rm eff}$, log g, [Fe/H], $v_{\rm t}$, abundances ([X/H]) for Mg, Ba, Eu, and their associated uncertainties.

(This table is available in its entirety in machine-readable form in the online article.)

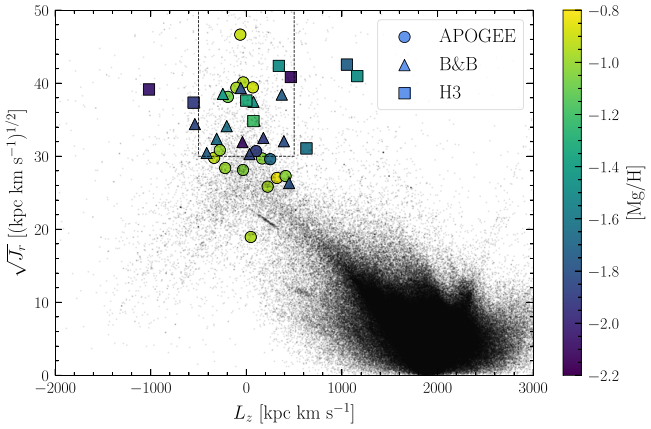

Figure 1. GSE sample in the $\sqrt{J_R}$ vs. L_z (defined as positive for prograde stars) space. The circles are the stars selected from APOGEE. The triangles are the stars selected from the Best & Brightest sample. The squares are the stars selected from the H3 survey. The D. K. Feuillet et al. (2020) selection box is shown with the dashed line. The stars are color coded by the measured [Mg/H]. APOGEE stars are shown as black dots for reference.

the distribution of the final sample in the $\sqrt{J_R}$ versus L_z space. The dynamical quantities are recalculated using the observed radial velocities measured in this study rather than those provided in the original surveys. As mentioned above, the D. K. Feuillet et al. (2020) selection shown in the figure is conservative and optimized for purity. Despite the different selections, most stars agree within 2σ of the strict selection region when considering the uncertainties of the calculated actions. Nonetheless, the rise in [Eu/Mg] is present even if we strictly remove the stars outside the selection region. Thus, the conclusions of this study remain unchanged if we were to adopt the same simple dynamical selection from D. K. Feuillet et al. (2020).

High-resolution optical spectra of 43 stars were obtained using the Magellan Clay 6.5 m Telescopes at Las Campanas Observatory using the Magellan Inamori Kyocera Echelle (MIKE) spectrograph (R. Bernstein et al. 2003) from 2021 July to December. Eleven stars were observed with the 0.″5 slit and 2×1 binning in 2021 July, yielding a resolution $R \sim 40{,}000/50{,}000$ on the blue/red arm of MIKE with wavelength coverage 3200–5000 and 4900–10000 Å, respectively. The other 32 stars were observed with the 0.″7 slit and 2×2 binning with a resolution $R \sim 28{,}000/22{,}000$. Table 1 describes the observational date, exposure time, and instrument setup for each observed target.

Stellar parameters were derived photometrically. The effective temperature ($T_{\rm eff}$) was determined using Gaia DR3 $G - RP$ colors (Gaia Collaboration et al. 2021) using color–[Fe/H]–$T_{\rm eff}$ relations from A. Mucciarelli et al. (2021). The metallicity ([M/H]) was set to be the average of Fe I line abundances measured using ATLAS model atmospheres from F. Castelli & R. L. Kurucz (2003), with [α/Fe] set equal to [Mg/Fe]. The surface gravity (log g) was determined by interpolating the Dartmouth isochrones along the red giant branch (A. Dotter et al. 2008). A pure spectroscopic analysis confirmed that these stars were all giant stars. Microturbulence ($v_{\rm t}$) was set to maintain a reduced equivalent width (REW) balance in Fe I. The derivation was iterated until the final photometric stellar parameters stabilized for each star.

The statistical uncertainties on $T_{\rm eff}$ and log g were determined by propagating input uncertainties through the color–[Fe/H]–$T_{\rm eff}$ relations and isochrone fitting, respectively. The [M/H] and $v_{\rm t}$ statistical uncertainties were determined from the standard error in [Fe I/H] and the slope with respect to REW, respectively. The systematic uncertainties for $T_{\rm eff}$, log g, [M/H], and $v_{\rm t}$ were set to 100 K, 0.2 dex, 0.2 dex, and 0.2 km s^{-1}. The final stellar parameters and associated total uncertainties for all 43 stars are included in Table 1.

We adopted the line list from R. P. Naidu et al. (2022) with all weak lines not measurable in metal-poor stars ([Fe/H] < -1.5) removed. For Eu, we measure the three lines at 4129, 4205, and 6645 Å in most of our stars. The spectra were analyzed using SMHR[7] (A. R. Casey 2014; A. P. Ji et al. 2020), which provides an interface for fitting equivalent widths, interpolating the stellar atmosphere models from F. Castelli & R. L. Kurucz (2003), running MOOG including scattering (C. A. Sneden 1973; J. S. Sobeck et al. 2011), and damping constants to determine abundances from equivalent widths and spectrum synthesis (P. S. Barklem et al. 2000). More details on the spectral analysis procedure and uncertainty treatment can be found in A. P. Ji et al. (2020). We show the final derived abundances in Table 1 and Figure 2.

3. Rise of the *r*-process

We first examine the α-element abundances [Mg/Fe] to further check on the GSE membership of the stars in our sample, in particular, whether they are accreted or in situ interlopers. P. E. Nissen & W. J. Schuster (2010) identified two distinct halo populations in the solar neighborhood with high-α and low-α abundances and associated them with in situ and

[7] https://github.com/andycasey/smhr

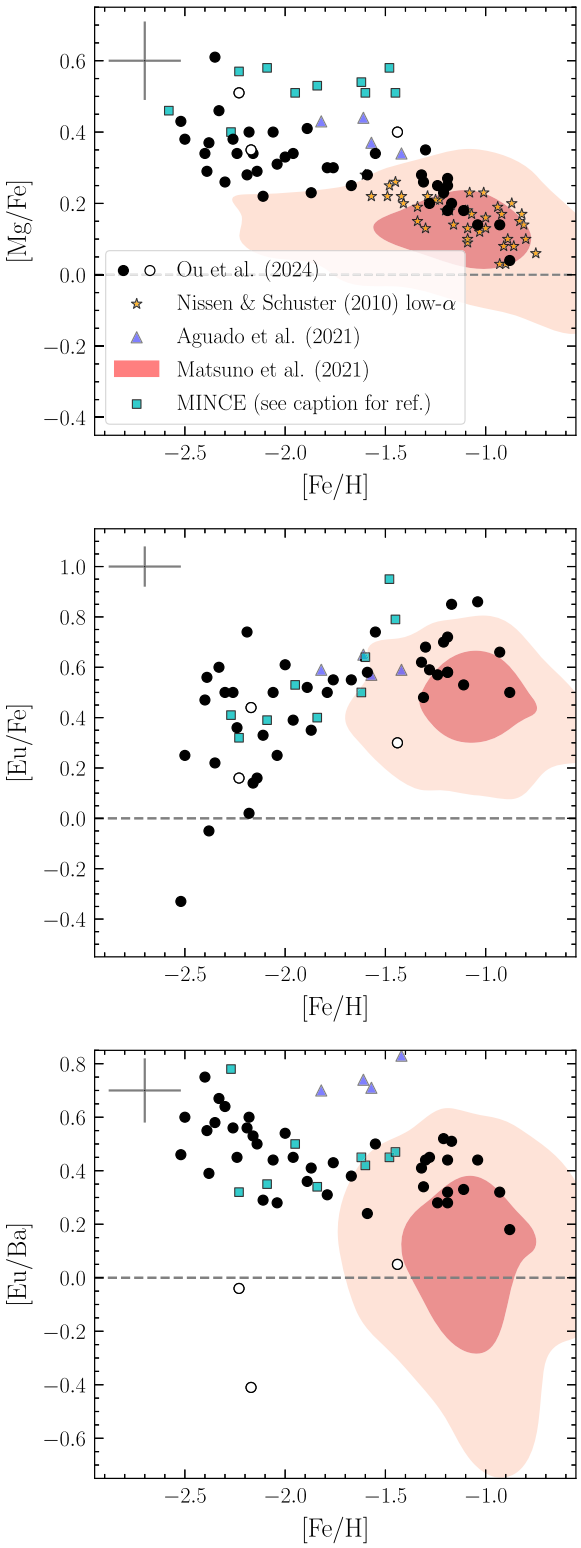

Figure 2. [Mg/Fe] (top), [Eu/Fe] (middle), and [Eu/Ba] (bottom) as a function of [Fe/H]. Measurements from this study are shown in black-filled/open circles. The typical uncertainties in the measurements are shown as the gray error bar in each panel. The orange stars are the low-α stars from P. E. Nissen & W. J. Schuster (2010). The blue triangles are the GSE stars from D. S. Aguado et al. (2021). The red contour shows the GSE stars from T. Matsuno et al. (2021). The cyan squares are the GSE stars from MINCE (G. Cescutti et al. 2022; P. François et al. 2024).

accreted origin, respectively. We take these populations as a benchmark for our sample. Comparing our measured [Mg/Fe] abundance with those from P. E. Nissen & W. J. Schuster (2010) shows that they are consistent with their low-α population stars.

Furthermore, comparisons between our sample with D. S. Aguado et al. (2021) and T. Matsuno et al. (2021), also targeting GSE stars, show overall good agreement. We observe a systematic offset when compared with G. Cescutti et al. (2022), with their [Mg/Fe] abundances systematically higher than other samples. This likely results from differences in stellar parameters, as G. Cescutti et al. (2022) have log g values $\sim$0.5 dex lower than APOGEE for cool stars (see their Figure 3). This 0.5 dex difference is sufficient to account for the systematic 0.2 dex offset in [Mg/Fe]. Overall these comparisons lend confidence that we have obtained a sufficiently pure GSE sample.

In the middle panel of Figure 2, we show the increase in [Eu/Fe] as a function of [Fe/H]. The metal-rich ([Fe/H] $\gtrsim -1.75$) part of the sample shows a consistently elevated mean value of [Eu/Fe] $= 0.62 \pm 0.02$ dex with a standard deviation $\sigma = 0.13$ dex. The same behavior was also found by D. S. Aguado et al. (2021), T. Matsuno et al. (2021), and P. François et al. (2024). The metal-poor sample ([Fe/H] $\lesssim -1.75$), on the other hand, exhibits a lower level of [Eu/Fe] $= 0.39 \pm 0.01$ ($\sigma = 0.22$) dex. Likewise, the mean [Eu/Mg] values at high and low [Mg/H] (divided at [Mg/H] $= -1.50$) are 0.32 ± 0.04 ($\sigma = 0.16$) and 0.05 ± 0.03 ($\sigma = 0.24$) dex, respectively. The rise in [Eu/Mg] as a function of [Mg/H] is thus statistically significant given the 0.27 dex mean difference and $\sim$0.03–0.04 dex error of the mean.

Most stars in our sample have large [Eu/Ba] ratios that indicate an r-process origin for these elements, bottom panel of Figure 2. In particular, the r-process nucleosynthesis predicts a ratio of [Eu/Ba] $= 0.8$ for a pure r-process origin (C. Sneden et al. 2008). Some of our stars fall near the [Eu/Ba] $= 0.8$ regime, while others have slightly lower values (between 0.2 and 0.6). This suggests that some s-process contribution is present in these stars, though the s-process contribution to Eu is low enough to be neglected. Three additional stars show signatures of significant s-process contribution, given their low [Eu/Ba] values of [Eu/Ba] $\lesssim 0.1$. We mark these stars as open circles in all figures and ignore them for studying r-process evolution.

In order to remove the effect of the delayed production of Fe by Type Ia SNe, we choose to consider [Eu/Mg] as a function of [Mg/H] (e.g., E. Tolstoy et al. 2009; Á. Skúladóttir & S. Salvadori 2020; G. Limberg et al. 2024) going forward. The evolution of the [Eu/Mg] is shown in Figure 3 and can be interpreted as the evolution of r-process elements as a function of time and star formation.

We find an increase in the mean [Eu/Mg], with [Eu/Mg] $= 0.05 \pm 0.03$ ($\sigma = 0.24$) and [Eu/Mg] $= 0.32 \pm 0.04$ ($\sigma = 0.16$) for stars with [Mg/H] < -1.5 and [Mg/H] > -1.5, respectively. Thus, for the first time, we observe a robust rise of [Eu/Mg] with decreasing scatter over the course of the star formation history in the GSE. The observed rising trend is strong evidence of delayed r-process sources, presumably NSMs.

4. Modeling the r-process Rise in the GSE

4.1. r-process Model with rCCSNe and NSMs

We model the rise in [Eu/Mg] as the result of two dominant r-process sites, prompt (rCCSNe) and delayed (NSMs) sources, and estimate the yields and delay time distribution necessary to

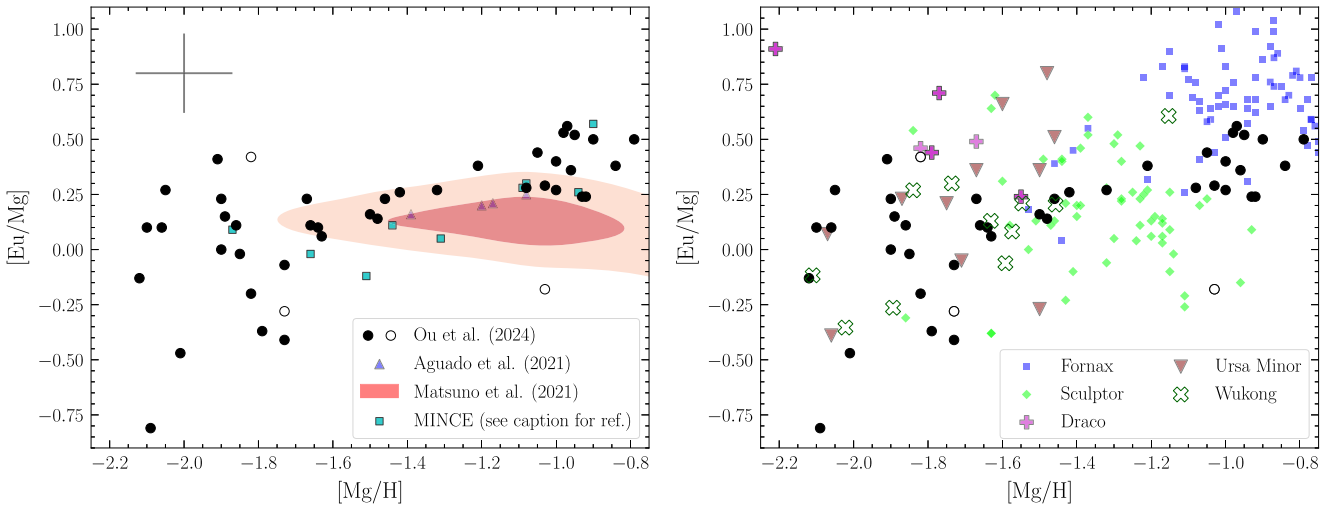

Figure 3. [Eu/Mg] as a function of [Mg/H]. Measurements from this study are shown in black-filled/open circles. The typical uncertainty of the measurements is shown as the gray error bar. The left panel compares our sample with other GSE *r*-process measurements (D. S. Aguado et al. 2021; T. Matsuno et al. 2021; G. Cescutti et al. 2022; P. François et al. 2024). The right panel compares our sample with other dwarf systems, with intact dwarfs Fornax, Sculptor, Draco, and Ursa Minor (compiled and taken from A. Frebel & A. P. Ji 2023), as well as the dissolved dwarf Wukong/LMS-1 sample (G. Limberg et al. 2024).

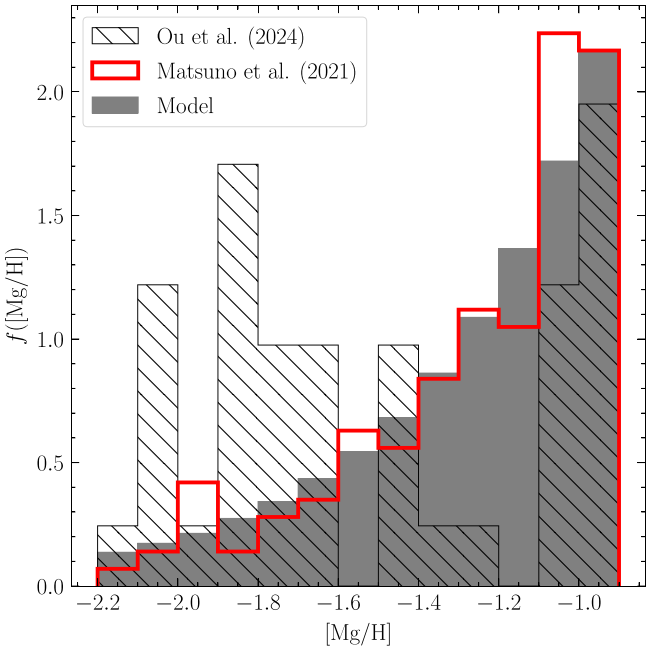

Figure 4. Comparison of the [Mg/H] distribution function from the model (gray solid) and data from this study (black hatched) and T. Matsuno et al. (2021; red open). The model produces [Mg/H] distribution function that is broadly consistent with that from T. Matsuno et al. (2021), a purely kinematically selected GSE sample.

reproduce the observed rise. To do so, we first build an empirical relation between [Mg/H] and age. Assuming the total mass of Mg in the GSE increases linearly with time, [Mg/H] increases logarithmically with time, i.e., the age of the star decreases exponentially with [Mg/H]. Given the infall time of the GSE (∼10 Gyr ago; e.g., A. Bonaca et al. 2020) and our sample with $-2.2 \lesssim [\mathrm{Mg/H}] \lesssim -0.8$, we construct the exponential relation:

$$\mathrm{Age} = -0.15 \times 10^{[\mathrm{Mg/H}]+2.2} + 14. \quad (3)$$

M. Xiang & H.-W. Rix (2022) obtained age estimates for subgiants by comparing the stars' locations to isochrones. We thus select GSE candidates from their sample following our dynamical space selections described in Section 2 for comparison. As shown in the top panels of Figure 5, assuming their [α/H] is the same as our [Mg/H], our relation is within the scatter of ages from M. Xiang & H.-W. Rix (2022) and provides a reasonable description of GSE's chemical enrichment history. We note that this conversion between [Mg/H] and age is intended only for estimating the timescale of the Eu abundance rise, and not for actually assigning ages to our GSE stars. Thus, stars with ages older than the Hubble time do not affect our ability to interpret the time evolution of the *r*-process in the GSE.

Our chemical evolution model is the same as the one introduced by R. P. Naidu et al. (2022). In short, the model describes the trend with rCCSNe, a prompt *r*-process site, and NSMs, a delayed *r*-process site producing Eu, as well as normal CCSNe producing Mg in a galaxy with a constant star formation rate. The normal CCSNe rate is set to produce [Mg/H] evolution consistent with the empirical relation between stellar age and [Mg/H]. The model qualitatively matches current constraints on the GSE: the [Mg/H] distribution in T. Matsuno et al. (2021; Figure 4), as well as the ages inferred by C. Gallart et al. (2019), F. Vincenzo et al. (2019), and A. Bonaca et al. (2020). For the prompt site, we assume a constant production rate of Eu as a function of time with an effective yield per one Myr of star formation ($y_{\mathrm{eff,p}}$). For the delayed site, we assume a power-law delay time distribution ($t_{\mathrm{delay}} \propto t^{-1.5}$; e.g., K. Paterson et al. 2020; M. Zevin et al. 2022)[8] with a minimum delay time ($t_{\mathrm{delay,min}}$) for the Eu production with effective yield per one Myr of star formation ($y_{\mathrm{eff,d}}$). $y_{\mathrm{eff,p}}$ and $y_{\mathrm{eff,d}}$ are determined both by the relative rate of rCCSNe (or NSMs) to CCSNe and the yield of individual rCCSNe (or NSMs). We thus have a total of three free parameters for the model: $y_{\mathrm{eff,p}}$, $y_{\mathrm{eff,d}}$, and $t_{\mathrm{delay,min}}$. Due to the degeneracies discussed below, in practice, we fix $t_{\mathrm{delay,min}}$ and set the effective yields to match the model to the data. For completeness, we note that our model [Eu/Mg] computations

[8] The power-law exponent choice between −1.5 and −1 has no significant impact on the conclusion of the analysis.

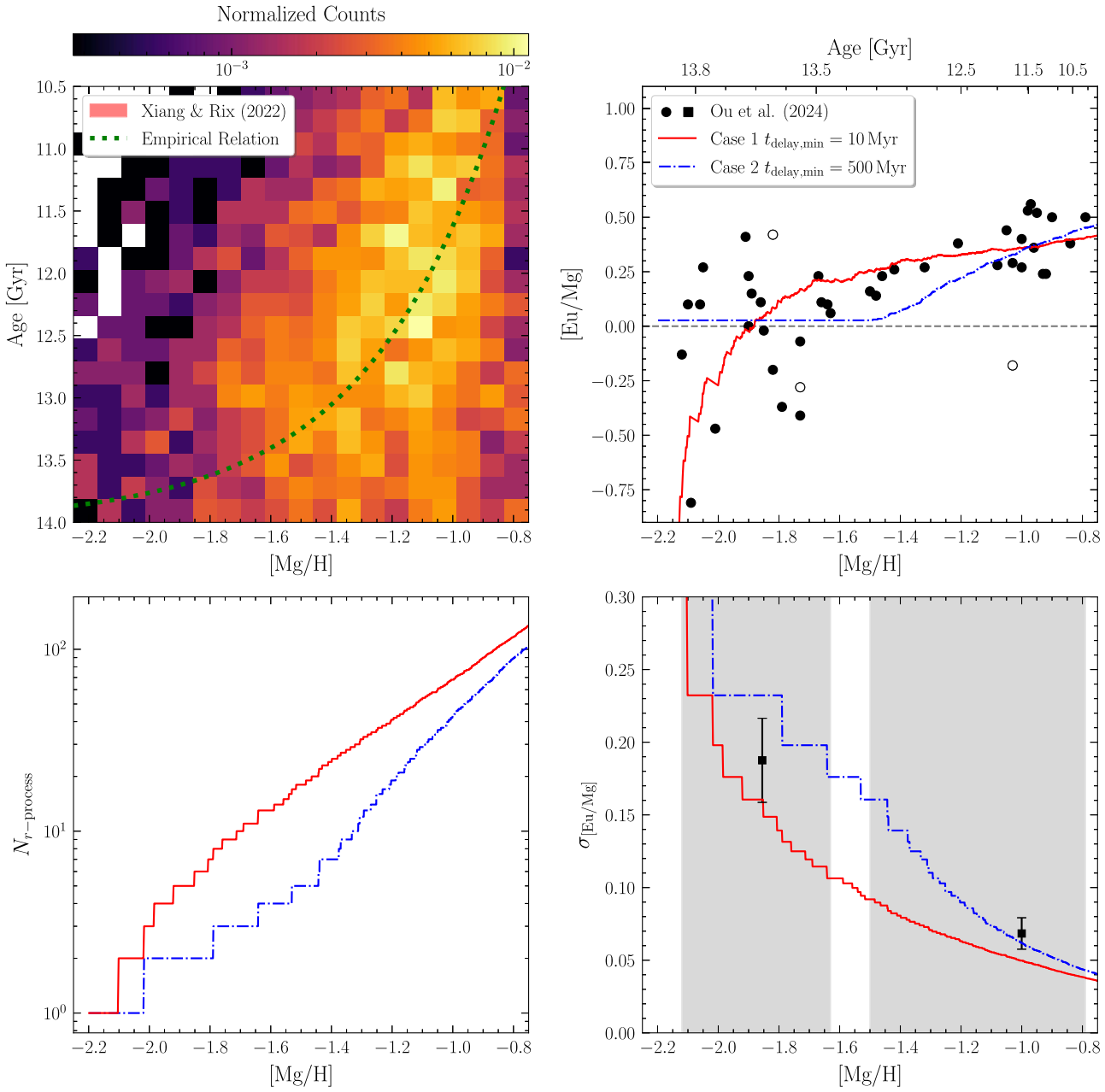

Figure 5. Comparison of our simple model with observational data. The model is further described in Section 4. The top left panel shows the empirical relation (green dashed line) between [α/H] and age compared with GSE candidates from M. Xiang & H.-W. Rix (2022). The 2D histogram shows the distribution of the stars in log scale. The top right panel shows two cases of our model (red solid line and blue dotted–dashed line) of the Eu enrichment process by rCCSNe+NSMs. The bottom left panel shows the corresponding number of *r*-process events for the two cases. The bottom right panel shows the observed (squares) and expected (lines) scatters in [Eu/Mg] as a function of [Mg/H]. The expected scatters are estimated from the number of *r*-process events based on Poisson statistics, while the observed scatters (after removing the typical measurement uncertainties in [Eu/Mg]) are calculated from two subsamples split up at [Mg/H] = −1.5. The vertical error bars represent the estimated uncertainties of the observed scatter. The shaded regions represent the range of [Mg/H] of the two subsamples, with the horizontal position of the squares marking the median [Mg/H].

are performed on a linear scale and then converted to a log scale for comparison with the observed data.

4.2. Two Cases and Inferred Yields

This model can reasonably describe the observed [Eu/Mg] trend with both short (10 Myr) and long (500 Myr) minimum delay time for NSMs, as shown in Figure 5, given the large scatter in [Eu/Mg] at ages older than 13 Gyr. With the short minimum delay time (Case 1; red line in the top right panel of Figure 5), we interpret the α-poor sample as a fast increase in [Eu/Mg] starting from the most α-poor stars, with a decreasing slope as age decreases. With the long minimum delay time (Case 2; blue line), we interpret the α-poor sample to be constant with a large scatter up to age 13 Gyr, as expected with only rCCSNe. In this case, [Eu/Mg] starts increasing after the NSMs have experienced the minimum delay time.

We find that the effective Eu yield for NSM is qualitatively the same in both cases. This is expected as the two cases are constrained to reach the same mean observed level of [Eu/Mg] at [Mg/H]> -1.2. At this [Mg/H] range, the Eu production is dominated by the NSM in either case and thus the total Eu yield

for these NSMs must be similar. Assuming a relative rate of NSM to CCSNe of $10^{-2.5}$, based on estimates for NSMs from gravitational wave observations (Abbott et al. 2024) and CCSNe from transient surveys (D. A. Perley et al. 2020), we get an Eu yield per NSM of $10^{-5.5}\,M_{\odot}$, consistent with estimates from GW170817 (B. Côté et al. 2018) and LIGO-Virgo-KAGRA NSM observations (H.-Y. Chen et al. 2024).

The biggest difference between the two cases is the Eu yield from rCCSNe. For Case 1, the short minimum delay scenario, we find that a much lower effective Eu yield from rCCSNe is required than the long minimum delay scenario model (Case 2). In other words, the rCCSNe do not need to produce nearly as much Eu if the NSMs start producing Eu with a short time delay. This is consistent with the fact that rCCSNe are invoked to provide early *r*-process production if NSMs experience a long delay time before their merger (e.g., F. Matteucci et al. 2014; D. M. Siegel et al. 2019). Assuming a relative rate of rCCSNe to CCSNe of 10^{-4}, consistent, e.g., with long gamma-ray burst rates (D. Guetta et al. 2005; D. Wanderman & T. Piran 2010; A. Lien et al. 2014), the Eu yield per rCCSNe is $\sim 5 \times 10^{-7}\,M_{\odot}$and $\sim 1 \times 10^{-5}\,M_{\odot}$in Case 1 and Case 2, respectively. The latter is consistent with results from D. M. Siegel et al. (2019) and K. Brauer et al. (2021), as expected for cases where collapsars can produce the Eu abundances observed in very metal-poor stars.

We emphasize again that the increasing [Eu/Mg] requires delayed *r*-process sources, regardless of the minimum delay time. Furthermore, as long as the effective Eu yield for NSM is fixed to match the final observed [Eu/Mg], the minimum delay time of NSMs can be reduced by decreasing the effective Eu yield for rCCSNe. The effective Eu yield of the rCCSNe is, therefore, degenerate with the minimum delay time of NSMs. Thus, fast mergers from NSMs mimic early rCCSNe, rendering the two indistinguishable from each other, as it may have occurred in the GSE. Future studies of even more metal-poor GSE stars are needed to constrain to what extent a rCCSNe component is needed.

4.3. Breaking the Degeneracy

The degeneracy in the minimum delay time can be broken with *r*-process measurements from other galaxies. R. P. Naidu et al. (2022) showed that the minimum delay time must be $\gtrsim$500 Myr by comparing the median [Eu/Mg] of stars from the GSE and Kraken, two disrupted dwarfs with a similar stellar mass but different stellar formation duration. We note that this alternative method relies on assumptions about the galaxies' star formation history and accretion time, and can only place a lower limit on the minimum delay time. However, the star formation history and accretion time for Kraken are relatively uncertain. Nonetheless, we may tentatively argue that Case 2 with a 500 Myr delay time for the NSMs and a higher rCCSNe *r*-process yield is preferred when taking the constraint from R. P. Naidu et al. (2022) into account.

The scatter in [Eu/Mg] can also break the degeneracy. The intrinsic rare nature of *r*-process events means that there must be a transition from early discrete stochastic enrichment ($\sim$a few events) to a late continuous evolution ($\sim$30 events; K. Brauer et al. 2021; A. Frebel & A. P. Ji 2023). While the onset of any delayed *r*-process sources increases the mean *r*-process element abundances, the overall transition from chemical enrichment to evolution tends to reduce the scatter around the mean. The bottom left panel of Figure 5 shows the expected total number of *r*-process events in the two cases.

We infer the intrinsic scatter in [Eu/Mg] based on Poisson statistics from the number of events, assuming no intrinsic variation in *r*-process events yield and there is instantaneous mixing. After accounting for typical measurement uncertainties ($\sim$0.15 dex), the observed scatter in [Eu/Mg] is qualitatively consistent with the values we found for either case, as shown in the bottom right panel of Figure 5. Further quantifying and constraining the total number of *r*-process events via the observed scatter in [Eu/Mg], however, requires a larger sample of stars at low [Mg/H] to improve the statistics, as well as considerations of intrinsic variation in *r*-process event yields (e.g., A. P. Ji et al. 2019)

4.4. Model Limitations

The simple model presented above is intended to illustrate the significance of the rise, not to provide rigorous constraints on the model parameters. In this section, we describe its assumptions and limitations, as well as possible directions of improvement for future studies. However, any modifications will not qualitatively change the presence of the *r*-process rise in GSE.

First, our chemical evolution models adopt an age–[Mg/H] relation from M. Xiang & H.-W. Rix (2022) with a constant star formation rate. There are more subtle and unmodeled features (e.g., the rapidity at which the star formation history quenches at 10 Gyr ago) that may affect the chemical evolution model results (J. W. Johnson & D. H. Weinberg 2020; G. Cescutti et al. 2022). For models based on a smooth nonconstant star formation history, the detailed form of the star formation history appears to have a minimal impact on the abundance trends of various elements predicted (J. W. Johnson & D. H. Weinberg 2020). Thus, these features may affect the detailed timescales of the [Eu/Mg] rise but not the presence of the rise itself.

Additionally, the two *r*-process sources in our model do not reflect the intrinsic scatter in *r*-process yields from specific sites or mixing lengths (see, e.g., G. Cescutti & C. Chiappini 2014; K. Brauer et al. 2021). We also assume that Mg is dominantly produced by ordinary CCSNe, whereas Eu is dominantly produced by prompt/delayed *r*-process sources. Therefore, our model is limited to three types of nucleosynthesis events and their impact on Mg and Eu production, unlike, for example, G. Cescutti et al. (2022) and P. François et al. (2024), who use all available elemental abundances to constrain multiple possible nucleosynthesis channels all at once. Yet, as shown in Section 4.2, even our simplistic model with three free parameters already shows degenerate behavior. Invoking more sophisticated models would inevitably add more degrees of freedom and likely make the interpretation more complex. Since the focus of this study is to establish and provide a straightforward interpretation of the *r*-process rise, we opt for the simpler model.

5. *r*-process in Other Dwarf Galaxies

We now consider available *r*-process abundances in intact and disrupted dwarf galaxies to establish to what extent other systems might also display the steep rise in [Eu/Mg] observed in the GSE.

In Figure 3, we compare *r*-process abundance measurements available for stars in other dwarf galaxies with our sample. For the most massive systems (stellar mass $M_\star > 10^6\,M_\odot$ from A. W. McConnachie 2012), Sculptor and Fornax, the stars roughly overlap with the GSE sample at high [Mg/H]. In particular, for Sculptor, measurements of the Eu abundances from V. Hill et al. (2019) established that the system has reached a constant [Eu/Mg] ~ 0.2 at higher metallicities. Yet, the existence of delayed *r*-process sources in Sculptor is still under debate because stars with actual Eu measurements remain lacking at [Mg/H] $\lesssim -1.6$ (G. E. Duggan et al. 2018; Á. Skúladóttir et al. 2019).

Likewise, Fornax (B. Letarte et al. 2010; B. Lemasle et al. 2014) shows a constant elevated level of [Eu/Mg] ~ 0.4, with no conclusive evidence of a change in [Eu/Fe]. Hence, there is no support for delayed sources in Fornax due to a lack of Eu measurements at lower metallicities.

On the other hand, the medium-mass ($M_\star \sim 10^{5.5}\,M_\odot$) dwarf galaxies, Draco and Ursa Minor, show more significant scatter and no clear trend compared to what we observed in the GSE. The large scatter suggests both systems are still in their stochastic enrichment stage (M. D. Shetrone et al. 2001; J. G. Cohen & W. Huang 2010; T. Tsujimoto et al. 2017; A. Frebel & A. P. Ji 2023), which prevents conclusive interpretation regarding the evolution of [Eu/Mg], although G. E. Duggan et al. (2018) argued for an increasing *r*-process trend in these galaxies, especially in Ursa Minor, using Ba measurements and an average trend in [Ba/Eu].

We also compare our results with measurements from the disrupted dwarf Wukong/LMS-1 stellar stream (R. P. Naidu et al. 2020; Z. Yuan et al. 2020) by G. Limberg et al. (2024). A similar rise in [Eu/Mg] as found in the GSE is observed in Wukong/LMS-1, though we note that stars from this accreted system are only found up to [Mg/H]~ -1.2. However, such a metallicity cutoff is expected given Wukong/LMS-1's lower estimated total mass, and hence, its lower star formation efficiency, when compared with GSE properties.

Recent observations of the Large Magellanic Cloud (LMC) also show potential support for delayed *r*-process sources (H. Reggiani et al. 2021; A. Chiti et al. 2024). For LMC stars at [Fe/H] > -2.5, H. Reggiani et al. (2021) measured *r*-process enhancement at the level of [Eu/Fe] ~ 0.7, while A. Chiti et al. (2024) found no evidence of *r*-process enhancement for LMC stars with [Fe/H] < -2.5. The comparison suggests that there may be a similar rise present in the LMC, with the delayed *r*-process sources changing the *r*-process enhancement level at [Fe/H] ~ -2.5.

In summary, no other dwarf galaxies, except for tentative evidence from Wukong/LMS-1 and LMC, currently display any similarly clear and obvious rise in [Eu/Mg] with [Mg/H] as the GSE does. Additional stellar data in the GSE and other systems will thus bring forward important clues about how the *r*-process rises within different galactic environments.

6. Conclusions

We study the *r*-process elements in a sample of 43 GSE stars with a metallicity ranging between [Fe/H] ~ -2.5 and -1.0. Eleven metal-poor stars with [Fe/H] $\lesssim -2.0$ allow us to probe the early *r*-process enrichment, previously out of reach. We also derive Eu and Mg abundances to study the evolution of *r*-process elements and their astrophysical sources in the GSE progenitor.

GSE is the second-ever dwarf galaxy for which we find a clear rise in [Eu/Mg]. Such a rise has been expected due to delayed *r*-process sources; yet evidence has only recently come to the surface.

We examine the rise of the *r*-process in two scenarios where the increase of observed *r*-process abundances may be explained either with (1) a short delay (10 Myr) in NSMs and with low-yield rCCSNe producing minimal *r*-process at early time, or with (2) a long delay (500 Myr) in NSMs and with high-yield rCCSNe producing all *r*-process elements at early time. Both cases require delayed *r*-process sources and predict effective Eu yields for different sites that are consistent with what is found in the literature. Prompt sources alone can explain *r*-process enrichment at early times but require yields close to the estimated Eu yield of a given NSM (B. Côté et al. 2018). If rCCSNe cannot supply enough *r*-process element enrichment, NSMs must correspondingly have a shorter delay time. These takeaways are independent of many degeneracies typically encountered in modeling chemical enrichment processes in galaxies.

This study showcases the power of using massive disrupted dwarf galaxies in the Milky Way halo to constrain early *r*-process enrichment and the astrophysical sites of the *r*-process. Systems like the GSE have stellar populations that are relatively easily accessible for obtaining high-resolution spectroscopy of member stars, and they have a less complex merger history than the Milky Way that makes these kinds of explorations possible. Multiple recent studies targeting the GSE have also observed this rise (H. Ernandes et al. 2024; P. François et al. 2024; S. Monty et al. 2024). Further constraining the delayed *r*-process sources' delay time distribution and combined element yields will rely on additional observations that probe the more metal-poor population in the GSE as well as other accreted dwarf galaxies.

Acknowledgments

X.O. thanks the LSST Discovery Alliance Data Science Fellowship Program, which is funded by LSST Discovery Alliance, NSF Cybertraining Grant #1829740, the Brinson Foundation, and the Moore Foundation; his participation in the program has benefited this work. X.O. and A.F. acknowledge support from NSF grants AST-1716251 and AST-2307436. A. P.J acknowledges support from NSF grants AST-2206264 and AST-2307599. G.L. acknowledges FAPESP (procs. 2021/10429-0 and 2022/07301-5).

This work presents results from the European Space Agency (ESA) space mission Gaia. Gaia data are being processed by the Gaia Data Processing and Analysis Consortium (DPAC). Funding for the DPAC is provided by national institutions, in particular, the institutions participating in the Gaia MultiLateral Agreement (MLA). The Gaia mission website is https://www.cosmos.esa.int/gaia. The Gaia archive website is https://archives.esac.esa.int/gaia.

This research has made use of NASA's Astrophysics Data System Bibliographic Services; the arXiv preprint server operated by Cornell University; the SIMBAD and VizieR databases hosted by the Strasbourg Astronomical Data Center.

Software: `matplotlib` (J. D. Hunter 2007), `numpy` (S. van der Walt et al. 2011), `scipy` (P. Virtanen et al. 2020), `astropy` (Astropy Collaboration et al. 2013, 2018), and `SMHR` (A. R. Casey 2014).

ORCID iDs

Xiaowei Ou (欧筱葳) https://orcid.org/0000-0002-4669-9967
Alexander P. Ji https://orcid.org/0000-0002-4863-8842
Anna Frebel https://orcid.org/0000-0002-2139-7145
Rohan P. Naidu https://orcid.org/0000-0003-3997-5705
Guilherme Limberg https://orcid.org/0000-0002-9269-8287

References

Abbott, R., et al. The LIGO Scientific Collaboration and The Virgo Collaboration 2024, PhRvD, 109, 022001
Aguado, D. S., Belokurov, V., Myeong, G. C., et al. 2021, ApJL, 908, L8
Astropy Collaboration, Price-Whelan, A. M., & Sipőcz, B. M. 2018, AJ, 156, 123
Astropy Collaboration, Robitaille, T. P., & Tollerud, E. J. 2013, A&A, 558, A33
Barklem, P. S., Piskunov, N., & O'Mara, B. J. 2000, A&AS, 142, 467
Belokurov, V., Erkal, D., Evans, N. W., Koposov, S. E., & Deason, A. J. 2018, MNRAS, 478, 611
Beniamini, P., & Piran, T. 2019, MNRAS, 487, 4847
Bernstein, R., Shectman, S. A., Gunnels, S. M., Mochnacki, S., & Athey, A. E. 2003, Proc. SPIE, 4841, 1694
Bonaca, A., Conroy, C., Cargile, P. A., et al. 2020, ApJL, 897, L18
Brauer, K., Ji, A. P., Drout, M. R., & Frebel, A. 2021, ApJ, 915, 81
Buder, S., Lind, K., Ness, M. K., et al. 2022, MNRAS, 510, 2407
Burbidge, E. M., Burbidge, G. R., Fowler, W. A., & Hoyle, F. 1957, RvMP, 29, 547
Casey, A. R. 2014, PhD Thesis, Australian National Univ.
Castelli, F., & Kurucz, R. L. 2003, in Modeling of Stellar Atmospheres, ed. N. Piskunov, W. W. Weiss, & D. F. Gray, Vol. 210 (San Francisco, CA: ASP), A20
Cescutti, G., Bonifacio, P., Caffau, E., et al. 2022, A&A, 668, A168
Cescutti, G., & Chiappini, C. 2014, A&A, 565, A51
Cescutti, G., Romano, D., Matteucci, F., Chiappini, C., & Hirschi, R. 2015, A&A, 577, A139
Chen, H.-Y., Landry, P., Read, J. S., & Siegel, D. M. 2024, arXiv:2402.03696
Chiti, A., Mardini, M., Limberg, G., et al. 2024, NatAs, 8, 637
Cohen, J. G., & Huang, W. 2010, ApJ, 719, 931
Conroy, C., Bonaca, A., Cargile, P., et al. 2019, ApJ, 883, 107
Côté, B., Fryer, C. L., Belczynski, K., et al. 2018, ApJ, 855, 99
Cowan, J. J., Sneden, C., Lawler, J. E., et al. 2021, RvMP, 93, 015002
da Silva, A. R., & Smiljanic, R. 2023, A&A, 677, A74
Dotter, A., Chaboyer, B., Jevremović, D., et al. 2008, ApJS, 178, 89
Drout, M. R., Piro, A. L., Shappee, B. J., et al. 2017, Sci, 358, 1570
Duggan, G. E., Kirby, E. N., Andrievsky, S. M., & Korotin, S. A. 2018, ApJ, 869, 50
Ernandes, H., Feuillet, D., Feltzing, S., & Skúladóttir, Á. 2024, arXiv:2405.13641
Ezzeddine, R., Rasmussen, K., Frebel, A., et al. 2020, ApJ, 898, 150
Feuillet, D. K., Feltzing, S., Sahlholdt, C. L., & Casagrande, L. 2020, MNRAS, 497, 109
François, P., Cescutti, G., Bonifacio, P., et al. 2024, A&A, 686, A295
Frebel, A. 2018, ARNPS, 68, 237
Frebel, A., & Ji, A. P. 2023, arXiv:2302.09188
Gaia Collaboration, Brown, A. G. A., & Vallenari, A. 2021, A&A, 649, A1
Gallart, C., Bernard, E. J., Brook, C. B., et al. 2019, NatAs, 3, 932
Guetta, D., Piran, T., & Waxman, E. 2005, ApJ, 619, 412
Hawkins, K., Jofré, P., Masseron, T., & Gilmore, G. 2015, MNRAS, 453, 758
Haywood, M., Di Matteo, P., Lehnert, M. D., et al. 2018, ApJ, 863, 113
Helmi, A., Babusiaux, C., Koppelman, H. H., et al. 2018, Natur, 563, 85
Hill, V., Skúladóttir, A. ´., Tolstoy, E., et al. 2019, A&A, 626, A15
Holmbeck, E. M., Hansen, T. T., Beers, T. C., et al. 2020, ApJS, 249, 30
Hunter, J. D. 2007, CSE, 9, 90
Ishimaru, Y., Wanajo, S., & Prantzos, N. 2015, ApJL, 804, L35
Ji, A. P., Drout, M. R., & Hansen, T. T. 2019, ApJ, 882, 40
Ji, A. P., Frebel, A., Chiti, A., & Simon, J. D. 2016, Natur, 531, 610
Ji, A. P., Li, T. S., Hansen, T. T., et al. 2020, AJ, 160, 181
Johnson, J. W., & Weinberg, D. H. 2020, MNRAS, 498, 1364
Jönsson, H., Holtzman, J. A., Allende Prieto, C., et al. 2020, AJ, 160, 120
Kasen, D., Metzger, B., Barnes, J., Quataert, E., & Ramirez-Ruiz, E. 2017, Natur, 551, 80
Kasliwal, M. M., Nakar, E., Singer, L. P., et al. 2017, Sci, 358, 1559
Kobayashi, C., Karakas, A. I., & Lugaro, M. 2020, ApJ, 900, 179
Kobayashi, C., Mandel, I., Belczynski, K., et al. 2023, ApJL, 943, L12
Kruijssen, J. M. D., Pfeffer, J. L., Chevance, M., et al. 2020, MNRAS, 498, 2472
Lemasle, B., de Boer, T. J. L., Hill, V., et al. 2014, A&A, 572, A88
Letarte, B., Hill, V., Tolstoy, E., et al. 2010, A&A, 523, A17
Lian, J., Storm, N., Guiglion, G., et al. 2023, MNRAS, 525, 1329
Lien, A., Sakamoto, T., Gehrels, N., et al. 2014, ApJ, 783, 24
Limberg, G., Ji, A. P., Naidu, R. P., et al. 2024, MNRAS, 530, 2512
Limberg, G., Santucci, R. M., Rossi, S., et al. 2021, ApJ, 913, 11
Limberg, G., Souza, S. O., Pérez-Villegas, A., et al. 2022, ApJ, 935, 109
Matsuno, T., Hirai, Y., Tarumi, Y., et al. 2021, A&A, 650, A110
Matteucci, F., Romano, D., Arcones, A., Korobkin, O., & Rosswog, S. 2014, MNRAS, 438, 2177
McConnachie, A. W. 2012, AJ, 144, 4
Monty, S., Belokurov, V., Sanders, J. L., et al. 2024, MNRAS, 533, 2420
Mösta, P., Roberts, L. F., Halevi, G., et al. 2018, ApJ, 864, 171
Mucciarelli, A., Bellazzini, M., & Massari, D. 2021, A&A, 653, A90
Naidu, R. P., Conroy, C., Bonaca, A., et al. 2020, ApJ, 901, 48
Naidu, R. P., Ji, A. P., Conroy, C., et al. 2022, ApJL, 926, L36
Nishimura, N., Takiwaki, T., & Thielemann, F.-K. 2015, ApJ, 810, 109
Nissen, P. E., & Schuster, W. J. 2010, A&A, 511, L10
Oh, W. S., Nordlander, T., Da Costa, G. S., Bessell, M. S., & Mackey, A. D. 2024, MNRAS, 528, 1065
Paterson, K., Fong, W., Nugent, A., et al. 2020, ApJL, 898, L32
Perley, D. A., Fremling, C., Sollerman, J., et al. 2020, ApJ, 904, 35
Placco, V. M., Santucci, R. M., Beers, T. C., et al. 2019, ApJ, 870, 122
Price-Whelan, A., Sipőcz, B., Starkman, N., et al. 2022, adrn/gala: v1.5, Zenodo, doi:10.5281/zenodo.6325733
Reggiani, H., Schlaufman, K. C., Casey, A. R., Simon, J. D., & Ji, A. P. 2021, AJ, 162, 229
Reichert, M., Hansen, C. J., Hanke, M., et al. 2020, A&A, 641, A127
Schlaufman, K. C., & Casey, A. R. 2014, ApJ, 797, 13
Shah, S. P., Ezzeddine, R., Roederer, I. U., et al. 2024, MNRAS, 529, 1917
Shetrone, M. D., Côté, P., & Sargent, W. L. W. 2001, ApJ, 548, 592
Siegel, D. M., Barnes, J., & Metzger, B. D. 2019, Natur, 569, 241
Simonetti, P., Matteucci, F., Greggio, L., & Cescutti, G. 2019, MNRAS, 486, 2896
Skúladóttir, Á., Hansen, C. J., Salvadori, S., & Choplin, A. 2019, A&A, 631, A171
Skúladóttir, Á., & Salvadori, S. 2020, A&A, 634, L2
Sneden, C., Cowan, J. J., & Gallino, R. 2008, ARA&A, 46, 241
Sneden, C. A. 1973, PhD Thesis, The Univ. of Texas at Austin
Sobeck, J. S., Kraft, R. P., Sneden, C., et al. 2011, AJ, 141, 175
Tolstoy, E., Hill, V., & Tosi, M. 2009, ARA&A, 47, 371
Tsujimoto, T., Matsuno, T., Aoki, W., Ishigaki, M. N., & Shigeyama, T. 2017, ApJL, 850, L12
Tsujimoto, T., & Shigeyama, T. 2014, ApJL, 795, L18
van der Walt, S., Colbert, S. C., & Varoquaux, G. 2011, CSE, 13, 22
Vigna-Gómez, A., Neijssel, C. J., Stevenson, S., et al. 2018, MNRAS, 481, 4009
Vincenzo, F., Spitoni, E., Calura, F., et al. 2019, MNRAS, 487, L47
Virtanen, P., Gommers, R., Oliphant, T. E., et al. 2020, SciPy: Open Source Scientific Tools for Python, Online, https://scipy.org/citing-scipy/
Wanderman, D., & Piran, T. 2010, MNRAS, 406, 1944
Winteler, C., Käppeli, R., Perego, A., et al. 2012, ApJL, 750, L22
Xiang, M., & Rix, H.-W. 2022, Natur, 603, 599
Yong, D., Kobayashi, C., Da Costa, G. S., et al. 2021, Natur, 595, 223
Yuan, Z., Chang, J., Beers, T. C., & Huang, Y. 2020, ApJL, 898, L37
Zevin, M., Nugent, A. E., Adhikari, S., et al. 2022, ApJL, 940, L18